



High-energy Neutrinos from Choked Gamma-Ray Bursts in Active Galactic Nucleus Accretion Disks

Jin-Ping Zhu¹ , Kai Wang² , Bing Zhang³ , Yuan-Pei Yang⁴ , Yun-Wei Yu⁵ , and He Gao⁶

¹ Department of Astronomy, School of Physics, Peking University, Beijing 100871, People's Republic of China; zhujp@pku.edu.cn

² Department of Astronomy, School of Physics, Huazhong University of Science and Technology, Wuhan 430074, People's Republic of China

³ Department of Physics and Astronomy, University of Nevada, Las Vegas, NV 89154, USA; zhang@physics.unlv.edu

⁴ South-Western Institute for Astronomy Research, Yunnan University, Kunming, Yunnan, People's Republic of China

⁵ Institute of Astrophysics, Central China Normal University, Wuhan 430079, People's Republic of China

⁶ Department of Astronomy, Beijing Normal University, Beijing 100875, People's Republic of China

Received 2021 March 5; revised 2021 March 26; accepted 2021 March 27; published 2021 April 16

Abstract

Both long-duration gamma-ray bursts (LGRBs) from the core collapse of massive stars and short-duration GRBs (SGRBs) from mergers of a binary neutron star or a neutron star–black hole are expected to occur in the accretion disk of active galactic nuclei (AGNs). We show that GRB jets embedded in the migration traps of AGN disks are promised to be choked by the dense disk material. Efficient shock acceleration of cosmic rays at the reverse shock is expected, and high-energy neutrinos would be produced. We find that these sources can effectively produce detectable TeV–PeV neutrinos through $p\gamma$ interactions. From a choked LGRB jet with isotropic equivalent energy of 10^{53} erg at 100 Mpc, one expects $\sim 2(7)$ neutrino events detectable by IceCube (IceCube-Gen2). The contribution from choked LGRBs to the observed diffuse neutrino background depends on the unknown local event rate density of these GRBs in AGN disks. For example, if the local event rate density of choked LGRBs in an AGN disk is $\sim 5\%$ that of low-luminosity GRBs ($\sim 10 \text{ Gpc}^{-3} \text{ yr}^{-1}$), the neutrinos from these events would contribute to $\sim 10\%$ of the observed diffuse neutrino background. Choked SGRBs in AGN disks are potential sources for future joint electromagnetic, neutrino, and gravitational wave multimessenger observations.

Unified Astronomy Thesaurus concepts: Cosmological neutrinos (338); Gamma-ray bursts (629); Neutron stars (1108); Black holes (162); Active galactic nuclei (16); Gravitational waves (678)

1. Introduction

Massive stars can be born in situ in an AGN accretion disk or be captured from the nuclear star cluster around the AGN (e.g., Artymowicz et al. 1993; Collin & Zahn 1999; Wang et al. 2011; Cantiello et al. 2021; Fabj et al. 2020; Dittmann et al. 2021). When they die, these massive stars will make supernovae (SNe) and leave behind NS and BH remnants inside the disk. Most of them might have extremely high spins and easily make LGRBs (Jermyn et al. 2021). Such embedded massive stars and stellar remnants would migrate inwards toward the trapping orbits within the disk (e.g., Bellovary et al. 2016; Tagawa et al. 2020). Abundant compact objects within the orbit would likely collide and merge (Cheng & Wang 1999; McKernan et al. 2020), which are the promising astrophysical gravitational wave (GW) sources for LIGO (Abbott et al. 2009). A possible SN (Assef et al. 2018) and a candidate binary black hole merger induced electromagnetic transient (Graham et al. 2020) have been reported recently in association with AGN disks.

GRBs, both long-duration ones associated with core collapse of massive stars (Woosley 1993; Galama et al. 1998; MacFadyen & Woosley 1999; Hjorth et al. 2003; Stanek et al. 2003; Zhang et al. 2003; Zhang & Mészáros 2004) and short-duration ones associated with neutron star mergers (Paczynski 1986, 1991; Eichler et al. 1989; Narayan et al. 1992; Abbott et al. 2017a, 2017b, 2017c) have been suggested as sources of astrophysical high-energy cosmic rays and neutrinos (Waxman & Bahcall 1997). On the other hand, nondetection of GRB neutrino signals (Icecube Collaboration et al. 2012; Aartsen et al. 2015b), likely related to a large emission radius from the central engine (Zhang &

Kumar 2013), suggested GRB-associated neutrinos can only account for at most $\lesssim 1\%$ of the diffuse neutrino fluence (Murase 2008; Wang & Dai 2009). The so-called low-luminosity GRBs are more abundant than successful ones (Liang et al. 2007; Sun et al. 2015) and can give significant contribution to the neutrino background (Murase & Nagataki 2006; Gupta & Zhang 2007). One possibility is that they originate from massive stars that launched jets that are choked in the stellar envelope (Bromberg et al. 2011a; Nakar 2015). Such choked jets from the death of massive stars or even from neutron star mergers could be more promising sites for efficient neutrino production, which may contribute to a considerable fraction of the diffuse neutrino background (Murase & Ioka 2013; Xiao & Dai 2014; Senno et al. 2016; Kimura et al. 2018; Fasano et al. 2021).

The presence of massive stars and compact binaries in AGN disks indicates that both LGRBs and SGRBs could possibly occur in such a high density environment. Very recently, Zhu et al. (2021) and Perna et al. (2021a) suggested that GRB jets in the AGN disks are likely choked,⁷ instead of making and resulting in observable signals from optical to γ -ray. In this work, we consider GRB jets choked inside the AGN disks as hidden sources of high-energy cosmic neutrinos, which can ease the tension between the diffuse extragalactic gamma-ray background and the diffuse background of TeV–PeV neutrinos.

⁷ Kimura et al. (2021) recently presented that compact binaries can accrete, produce radiation-driven outflows, and create cavities in the AGN disks before the merger, so that aligned SGRB jets could successfully break out from the AGN disks.

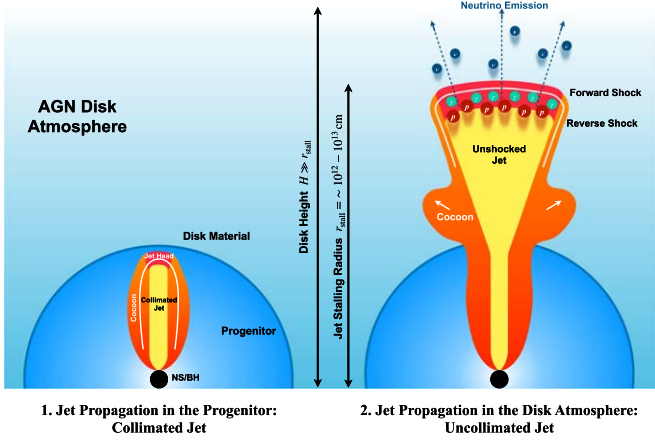


Figure 1. Schematic picture of jet propagation in the progenitor and in the AGN disk.

2. Jet Dynamics in AGN Accretion Disks

SNe and neutron star mergers are expected to occur in the migration traps (Bellovary et al. 2016) plausibly located at $a \sim 10^3 r_g$, where $r_g \equiv GM_{\text{SMBH}}/c^2$, G is the gravitational constant, M_{SMBH} is the AGN supermassive BH mass, and c is the speed of light. For a gas-pressure-dominated disk, the disk density is $\rho(z) = \rho_0 \exp(-z/H)$, where ρ_0 is the midplane density, z is the vertical distance, and $H = 1.5 \times 10^{14} M_{\text{SMBH},8\odot} \left(\frac{H/a}{0.01} \right) \left(\frac{a}{10^3 r_g} \right)$ is the disk height with the disk aspect ratio $H/a \sim [10^{-3}, 0.1]$ (Goodman & Tan 2004; Thompson et al. 2005). Near the migration traps, the midplane density is almost $\rho_0 \sim O(10^{-10}) \text{g cm}^{-3}$ and the disk height is $H \sim O(10^{14}) \text{cm}$. For a disk with an exponentially decaying density profile, the density $\rho \approx \rho_0$ for $z < H$, while ρ decreases rapidly for $z > H$. Therefore, for simplicity we approximately adopt a uniform density profile for the AGN disk for $z < H$. Hereafter, the convention $Q_x = Q/10^x$ is adopted in cgs units.

Figure 1 illustrates the physical processes for a jet traveling through the progenitor star and the AGN accretion disk. When a jet initially propagates inside the progenitor star, the collision between the jet and the stellar gas medium leads to the formation of a forward shock sweeping into the medium and a reverse shock entering the jet material (e.g., Matzner 2003; Bromberg et al. 2011b; Yu 2020). Such a structure is known as the jet head. The hot material that enters the head flows sideways and produces a powerful cocoon to drive a collimation shock into the jet material. The jet is collimated inside the star and gets accelerated to a relativistic velocity after it breaks out from the progenitor star.

After the jet enters into the AGN disk, the jet head velocity is given by Matzner (2003): $\beta_h = \beta_j / (1 + \tilde{L}^{-1/2})$, where $\beta_j \simeq 1$ and $\tilde{L} \equiv L_j / \pi r_j^2 \rho_0 c^3 \approx (10^{14} \text{cm}/r_j)^2 L_{j,50} \rho_{0,-10}^{-1}$ is the critical parameter that determines the evolution of the jet (Bromberg et al. 2011b), L_j is the jet luminosity, and r_j is the radius of the jet from the central engine. Since this jet radius should be $r_j \ll 10^{14} \text{cm}$, one gets $\tilde{L} > \theta_0^{-4/3} \gg 1$, where $\theta_0 \approx 0.2$. In this case, the jet head would travel with a relativistic speed. The cocoon pressure is too weak to affect the geometry of the jet so that the jet is uncollimated (i.e., $\theta_j \approx \theta_0$) (Bromberg et al. 2011b). Therefore, the critical parameter can be expressed as $\tilde{L} = L_{\text{iso}} / 2\pi r_h^2 \rho_0 c^3$, where $L_{\text{iso}} \approx 2L_j / \theta_0^2$ is the isotropic-equivalent one-side jet luminosity and $r_h \approx r_j / \theta_0$ is the distance between the jet head and the central engine. The Lorentz factor

of the jet head is given by $\Gamma_h \approx \tilde{L}^{1/4} / \sqrt{2}$. The internal energy and density evolution of the forward shock and reverse shock can be described by the shock jump conditions (Blandford & McKee 1976; Sari & Piran 1995; Zhang 2018):

$$\begin{aligned} e'_f / n'_f m_p c^2 &= \Gamma_h - 1, \quad n'_f / n_a = (\hat{\gamma}_1 \Gamma_h + 1) / (\hat{\gamma}_1 - 1) \\ &= 4\Gamma_h, \\ e'_r / n'_r m_p c^2 &= \bar{\Gamma}_h - 1, \quad n'_r / n'_j = (\hat{\gamma}_2 \bar{\Gamma}_h + 1) / (\hat{\gamma}_2 - 1) \\ &= 4\bar{\Gamma}_h, \end{aligned} \quad (1)$$

where $\hat{\gamma}_1 = (4\Gamma_h + 1) / 3\Gamma_h$, $\hat{\gamma}_2 = (4\bar{\Gamma}_h + 1) / 3\bar{\Gamma}_h$, the subscripts ‘‘a,’’ ‘‘f,’’ ‘‘r,’’ and ‘‘j’’ represent regions of the unshocked AGN material, the jet head’s forward shock, the jet head’s reverse shock, and the unshocked jet, and $\bar{\Gamma}_h = \Gamma_j \Gamma_h (1 - \beta_j \beta_h) \approx \Gamma_j \tilde{L}^{-1/4} / \sqrt{2}$ is the Lorentz factor of the unshocked jet measured in the jet head frame. Note we distinguish among three reference frames: Q for the AGN rest frame, Q' for the jet head comoving frame, and Q'' for the jet comoving frame.

We assume that a luminous jet can easily break out from the progenitor star, which has a similar parameter distribution as classical GRBs. Observationally, the average duration for LGRBs is $t_j \approx 10^{1.5} \text{s}$ (Kouveliotou et al. 1993; Horváth 2002; Zhang 2018) while the median isotropic energy release is $E_{\text{iso}} \approx 10^{53} \text{erg}$ for LGRB jets (the isotropic equivalent luminosity $L_{\text{iso}} = E_{\text{iso}}/t_j$) (Kumar & Zhang 2015). The jet could be choked in the AGN disk when the central engine quenches so that the jet head radius at t_j can be defined as the stalling radius, i.e., $r_{\text{stall}} = r_h(t_j) \approx 2\Gamma_h^2 c t_j = 2.0 \times 10^{13} E_{\text{iso},53}^{1/4} t_{j,1.5}^{1/4} \rho_{0,-10}^{-1/4} \text{cm}$, with $\Gamma_h = 2.7 E_{\text{iso},53}^{1/8} t_{j,1.5}^{-3/8} \rho_{0,-10}^{-1/8}$. For SGRB jets, the average duration and the median isotropic energy are $t_j \approx 10^{-0.1} \text{s}$ and $E_{\text{iso}} \approx 10^{51} \text{erg}$ (Fong et al. 2015), respectively. The stalling radius for the SGRB jet is $r_{\text{stall}} = 2.5 \times 10^{12} E_{\text{iso},51}^{1/4} t_{j,-0.1}^{1/4} \rho_{0,-10}^{-1/4} \text{cm}$ and the jet head Lorentz factor when it chokes is $\Gamma_h = 6.1 E_{\text{iso},51}^{1/8} t_{j,-0.1}^{-3/8} \rho_{0,-10}^{-1/8}$. Because $r_{\text{stall}} \ll H$, both LGRB and SGRB jets can be easily choked in an AGN accretion disk.

3. Neutrino Production

We assume that the Fermi acceleration operates and accelerated protons have a power-law distribution in energy: $dn_p/d\epsilon_p \propto \epsilon_p^{-s}$ with $s=2$ (Achterberg et al. 2001; Keshet & Waxman 2005). Here, the thermal photons from the jet head are treated as the only background photon field for hadronic interactions since the number densities of other types of radiation (e.g., the classical keV–MeV emission of GRBs) are typically much lower (Senno et al. 2016). Based on Equation (1), the internal energy and proton energy density of the jet head can be expressed as $e'_r = (\bar{\Gamma}_h - 1)n'_r m_p c^2$ and $n'_p = 4\bar{\Gamma}_h n'_j$, where m_p is the proton mass and $n'_j = L_{\text{iso}} / 4\pi \Gamma_j^2 r_{\text{stall}}^2 m_p c^3$ is the jet density. The photon temperature of the jet head is $k_B T'_r = (15\hbar^3 c^3 \epsilon_e e'_r / \pi^2)^{1/4}$, where $\epsilon_e \approx 0.1$ is the electron energy fraction. For classical parameters of LGRB (SGRB) jets, $k_B T'_r \approx 0.21 (0.32) \text{keV}$. One can obtain the average thermal photon energy $\epsilon'_\gamma = 2.7 k_B T'_r$ and the average thermal photon density $n'_\gamma = \epsilon_e e'_r / \epsilon'_\gamma$.

For the reverse shock, efficient Fermi acceleration can occur only if the radiation constraint (Murase & Ioka 2013) is

satisfied, i.e., $\tau_T = n''_j \sigma_T r_{\text{stall}} / \Gamma_j \lesssim \min[1, 0.1 C^{-1} \bar{\Gamma}_h]$, where $C = 1 + 2 \ln \bar{\Gamma}_h^2$. By considering $\Gamma_j = 300$ (500) for LGRB (SGRB) jets, we get $\tau_T = 6.8 \times 10^{-3} E_{\text{iso},53}^{3/4} t_{j,1.5}^{-5/4} \rho_{0,-10}^{1/4} \Gamma_{j,2.5}^{-3} \ll 0.32 C_{1.2}^{-1} \bar{\Gamma}_{h,1.7} \ll 1$ ($\tau_T = 4.6 \times 10^{-3} E_{\text{iso},51}^{3/4} t_{j,-0.1}^{-5/4} \rho_{0,-10}^{1/4} \Gamma_{j,2.7}^{-3} \ll 0.26 C_{1.2}^{-1} \bar{\Gamma}_{h,1.6} \ll 1$), which means that Fermi acceleration is always effective. Note that different from Senno et al. (2016) whose protons are from the internal shocks, the interacted protons in our calculations are accelerated from the reverse shock.

With the assumption of perfectly efficient acceleration, the acceleration timescale is given by $t'_{p,\text{acc}} = \epsilon'_p / (eB'c)$, where the jet head comoving magnetic field strength is $B' = \sqrt{8\pi\epsilon_B e'_r} \approx (\bar{\Gamma}_h / \Gamma_j) (8\epsilon_B L_{\text{iso}} / r_{\text{stall}}^2 c)^{1/2}$ and the magnetic field energy fraction is assumed as $\epsilon_B = 0.1$.

A high-energy proton loses its energy through radiative, hadronic, and adiabatic processes. The radiative cooling mechanisms contain synchrotron radiation with cooling timescale

$$t'_{p,\text{syn}} = \frac{6\pi m_p^4 c^3}{\sigma_T m_e^2 B'^2 \epsilon'_p}, \quad (2)$$

and inverse-Compton scattering with cooling timescale

$$t'_{p,\text{IC}} = \begin{cases} \frac{3m_p^4 c^3}{4\sigma_T m_e^2 n'_\gamma \epsilon'_p}, & \epsilon'_\gamma \epsilon'_p < m_p^2 c^4, \\ \frac{3\epsilon'_\gamma \epsilon'_p}{4\sigma_T m_e^2 c^5 n'_\gamma}, & \epsilon'_\gamma \epsilon'_p > m_p^2 c^4. \end{cases} \quad (3)$$

The hadronic cooling mechanisms mainly include the inelastic hadronuclear scattering (pp), the Bethe–Heitler pair production ($p\gamma \rightarrow pe^+e^-$), and the photomeson production ($p\gamma$). High-energy neutrinos are expected to be produced via pp and $p\gamma$ processes. The cooling timescale of pp scattering is given by $t'_{p,pp} = 1/c\sigma_{pp} n'_p \kappa_{pp}$, where the inelasticity is set as $\kappa_{pp} \simeq 0.5$ and the cross section σ_{pp} is obtained from Kelner et al. (2006). The energy loss rate of $p\gamma$ production is calculated by the formula given in Stecker (1968) and Murase (2007), i.e.,

$$t'_{p,p\gamma}^{-1} = \frac{c}{2\gamma_p} \int_{\bar{\epsilon}_{\text{th}}}^{\infty} d\bar{\epsilon} \sigma_{p\gamma}(\bar{\epsilon}) \kappa_{p\gamma}(\bar{\epsilon}) \bar{\epsilon} \int_{\bar{\epsilon}/2\gamma_p}^{\infty} d\epsilon \epsilon^{-2} \frac{dn}{d\epsilon}, \quad (4)$$

where $\bar{\epsilon}$ represents the photon energy in the rest frame of the proton, $\bar{\epsilon}_{\text{th}} \simeq 145$ MeV is the threshold energy, $\gamma_p = \epsilon'_p / m_p c^2$, and $dn/d\epsilon$ is the photon number density in the energy range of ϵ to $\epsilon + d\epsilon$. The inelasticity $\kappa_{p\gamma}$ and the cross section $\sigma_{p\gamma}$ are taken from Stecker (1968) and Patrignani et al. (2016). The energy loss rate of the Bethe–Heitler process t'_{BH}^{-1} can be also estimated based on Equation (4) by using κ_{BH} and σ_{BH} instead of $\kappa_{p\gamma}$ and $\sigma_{p\gamma}$. κ_{BH} , σ_{BH} , and $\bar{\epsilon}_{\text{th}}$ for the Bethe–Heitler process are adopted from Chodorowski et al. (1992).

Finally, the timescale for protons to lose energy due to adiabatic cooling is $t'_{p,\text{adi}} = r_{\text{stall}} / c\bar{\Gamma}_h$. We present the acceleration and cooling timescales of a choked LGRB and SGRB jet in an AGN disk in Figure 2. For both cases, pp scattering would dominate the cooling process for low-energy protons. The Bethe–Heitler process leads and suppresses neutrino production if the energy of protons falls within the range of 0.5 TeV $\lesssim \epsilon'_p \lesssim 20$ TeV. At higher energies, the dominant cooling mechanism for protons is $p\gamma$ interaction, which also limits the maximum proton energy to $\epsilon'_{p,\text{max}} \sim 10$ PeV.

Pions and kaons created through pp and $p\gamma$ processes decay into muons and muon neutrinos. Pions and kaons are subject to hadronic scattering, $t'_{(\pi,K),\text{had}} = 1/c\sigma_h n'_p \kappa_h$, where $\sigma_h \approx 5 \times 10^{-26}$ cm² and $\kappa_h \approx 0.8$ (Olive & Particle Data Group 2014). The intermediate muons then decay to muon neutrinos, electron neutrinos, and electrons. Similar to protons, pions, kaons, and muons also experience radiative processes and adiabatic cooling. One can calculate the synchrotron and IC cooling timescales of pions, kaons, and muons by Equations (2) and (3) with $\epsilon'_p \rightarrow \epsilon'_i$ and $m_p \rightarrow m_i$, where $i = \pi, K, \mu_\pi$, and μ_K are the parent particles for the neutrinos. The energy fractions from a proton to intermediate particles are calculated according to Denton & Tamborra (2018). By comparing these cooling timescales with the decay timescales of intermediate particles, i.e., $t_{i,\text{dec}} = \gamma_i \tau_i$ (where $\gamma_i = \epsilon'_i / m_i c^2$ and τ_i are the Lorentz factor and the rest frame lifetime, respectively), the final neutrino spectrum can be obtained.

Since both pp and $p\gamma$ processes produce neutrinos while other proton cooling processes suppress the final neutrino spectrum, the suppression factor taking into account various proton cooling processes is expressed as (Murase 2008; Wang & Dai 2009; Xiao et al. 2016) $\zeta_{p,\text{sup}}(\epsilon_{\nu_i}) = (t'^{-1}_{p,pp} + t'^{-1}_{p,p\gamma}) / t'^{-1}_{p,\text{cool}}$, where $t'^{-1}_{p,\text{cool}} = t'^{-1}_{p,pp} + t'^{-1}_{p,p\gamma} + t'^{-1}_{p,\text{BH}} + t'^{-1}_{p,\text{syn}} + t'^{-1}_{p,\text{IC}} + t'^{-1}_{p,\text{adi}}$. Similarly, the suppression factor due to meson cooling can be written as $\zeta_{i,\text{sup}}(\epsilon_{\nu_i}) = t'^{-1}_{i,\text{dec}} / t'^{-1}_{i,\text{cool}}$, where $t'^{-1}_{i,\text{cool}} = t'^{-1}_{i,\text{dec}} + t'^{-1}_{i,\text{had}} + t'^{-1}_{i,\text{syn}} + t'^{-1}_{i,\text{IC}} + t'^{-1}_{i,\text{adi}}$. One can obtain the neutrino spectrum in each neutrino production channel for a single event,

$$\epsilon_{\nu_i}^2 F_{\nu_i} = \frac{N_i E_{\text{iso}} \zeta_{p,\text{sup}}(\epsilon_{\nu_i}) \zeta_{i,\text{sup}}(\epsilon_{\nu_i})}{4\pi D_L^2 \ln(\epsilon'_{p,\text{max}} / \epsilon'_{p,\text{min}})}, \quad (5)$$

where $N_\pi = N_{\mu_\pi} = 0.12$, $N_K = 0.009$, and $N_{\mu_K} = 0.003$, the neutrino energy is $\epsilon_{\nu_i} = a_i \bar{\Gamma}_h \epsilon'_p$ with $a_\pi = a_{\mu_\pi} = 0.05$, $a_K = 0.10$, and $a_{\mu_K} = 0.033$, where D_L is the luminosity distance, and $\ln(\epsilon'_{p,\text{max}} / \epsilon'_{p,\text{min}})$ is the normalized factor with $\epsilon'_{p,\text{min}} \approx \bar{\Gamma}_h m_p c^2$. Highly efficient acceleration is assumed here (i.e., the acceleration efficiency $\zeta_p \simeq 1$) so that $\epsilon_{\text{acc}} \approx \zeta_p (1 - \epsilon_e - \epsilon_B) \approx 0.8 \sim 1$ which is in accord with the fiducial value of the baryon loading parameter $\zeta_{\text{acc}} \simeq \epsilon_{\text{acc}} / \epsilon_e \approx 10$ (Murase 2007).

Figure 3 shows the all-flavor fluence of a single burst at $D_L = 100$ Mpc. The fluence is mainly determined by the isotropic energy. The dip around a few TeV is caused by the suppression of neutrino production due to the Bethe–Heitler process. Low-energy neutrinos are dominated by pp interactions, and the neutrino spectrum above ~ 1 TeV that we are interested in mainly attributes to $p\gamma$ interactions. Both pp and $p\gamma$ processes are efficient as shown in Figure 3, since both the pp optical depth $n_p \sigma_{pp} r_{\text{stall}} / \bar{\Gamma}_h \sim 40(25)$ and the $p\gamma$ optical depth $n_\gamma \sigma_{p\gamma} r_{\text{stall}} / \bar{\Gamma}_h \sim 10^6 (2 \times 10^5)$ for a classical LGRB (SGRB) are quite large (Murase 2008; considering $\sigma_{pp} \approx 5 \times 10^{-26}$ cm² and $\sigma_{p\gamma} \approx 5 \times 10^{-28}$ cm² Particle Data Group et al. 2004, for rough estimations).

4. Neutrino Burst Detection

The expected number of muon neutrinos ν_μ from an on-axis GRB event detectable by IceCube and IceCube-Gen2 (Gen2)

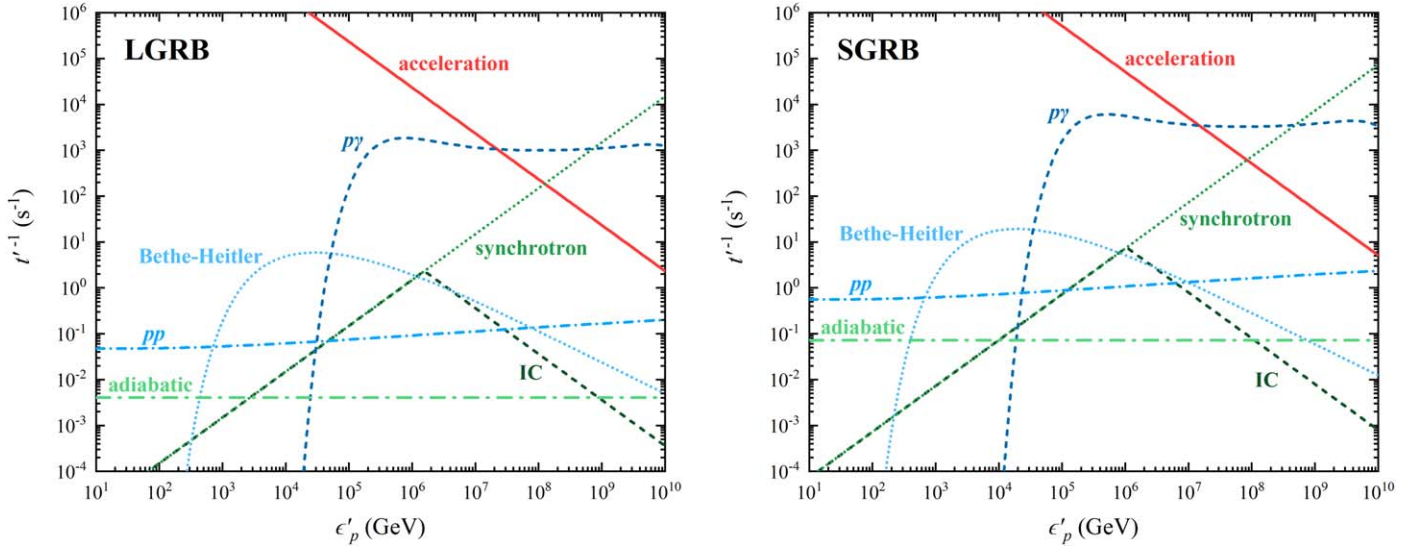


Figure 2. Inverse of proton acceleration and cooling timescales as a function of proton energy in the jet head frame for a classical LGRB (left panel) and SGRB (right panel). Acceleration (red solid), photomeson production ($p\gamma$, blue dashed), Bethe–Heitler pair production (blue dotted), hadronuclear scattering (pp , blue dashed-dotted), inverse-Compton (IC, green dashed), synchrotron radiation (green dotted), and adiabatic cooling (green dashed-dotted) processes are considered.

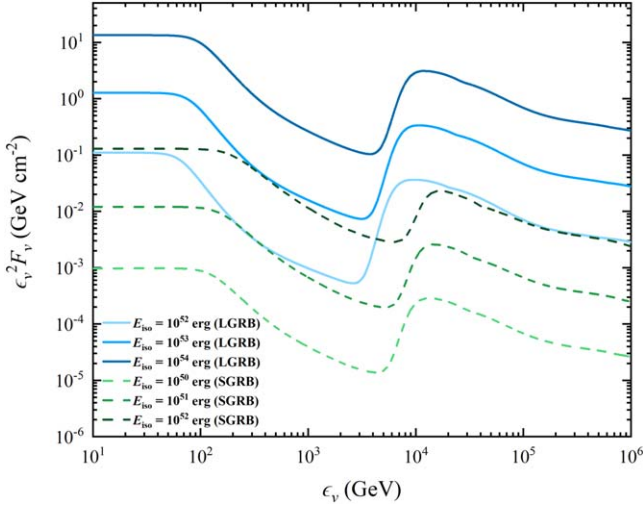


Figure 3. Expected all-flavor neutrino fluence as a function of neutrino energy ϵ_ν for GRBs at $D_L = 100$ Mpc. The three solid curves from light blue to dark blue are for choked LGRBs with three different isotropic jet energies: $E_{\text{iso}} = 10^{52}$, 10^{53} , and 10^{54} erg. The three dashed curves from light green to dark green are for choked SGRBs with three different isotropic jet energies: $E_{\text{iso}} = 10^{50}$, 10^{51} , and 10^{52} erg.

can be calculated by

$$N(\epsilon_\nu > 1 \text{ TeV}) = \int_{1 \text{ TeV}}^{\epsilon_{\nu, \text{max}}} d\epsilon_\nu F_\nu(\epsilon_\nu) A_{\text{eff}}(\epsilon_\nu), \quad (6)$$

where A_{eff} is the effective area of the detector. We obtain the effective areas of IceCube for the up- and down-going events from Aartsen et al. (2017). The effective volume of the Gen2 is larger than that of IceCube by a factor of ~ 10 , corresponding to a factor of $\sim 10^{2/3}$ times larger in the effective area (Aartsen et al. 2017). The number of detected ν_μ (e.g., Harrison et al. 2002) from a single event located at 100 Mpc are shown in Table 1 (after considering neutrino oscillation). If a classical LGRB occurs in an AGN disk at 100 Mpc, we expect $\sim 2(7)$ neutrino events from a single event detected by IceCube (Gen2). The neutrino flux from an SGRB is lower, and the

Table 1
Neutrino Burst Detection

Number of Detected ν_μ from Single Event at 100 Mpc			
Model ($E_{\text{iso}}/\text{erg}$)	IceCube (Up)	IceCube (Down)	Gen2(Up)
LGRB (10^{52})	0.16	0.016	0.76
LGRB (10^{53})	1.5	0.15	6.8
LGRB (10^{54})	13	1.4	61
SGRB (10^{50})	1.2×10^{-3}	1.4×10^{-4}	5.7×10^{-3}
SGRB (10^{51})	0.011	1.3×10^{-3}	0.050
SGRB (10^{52})	0.094	0.012	0.44
Joint GW + Neutrino Detection Rate			
Era(GW/Neutrino)		Detection Rate (yr^{-1})	
O4/IceCube		$f_{\text{AGN}}[0.006, 1.3] \times 10^{-1}$	
O5/IceCube		$f_{\text{AGN}}[0.007, 1.3] \times 10^{-1}$	
Voyager/Gen2		$f_{\text{AGN}}[0.041, 8.0] \times 10^{-1}$	
ET/Gen2		$f_{\text{AGN}}[0.042, 8.8] \times 10^{-1}$	

detection for a single choked SGRB is possible only with Gen2 given that the SGRB has a high energy and occurs in the Northern Hemisphere.

We simulate the joint GW+neutrino detection rate for neutron star mergers occurring in AGN disks. McKernan et al. (2020) showed that the local event rate densities $\dot{\rho}_0$ for BNS and NSBH mergers in the AGN channel are $\dot{\rho}_{0, \text{BNS}} \sim f_{\text{AGN}} [0.2, 400] \text{ Gpc}^{-3} \text{ yr}^{-1}$ and $\dot{\rho}_{0, \text{NSBH}} \sim f_{\text{AGN}} [10, 300] \text{ Gpc}^{-3} \text{ yr}^{-1}$, respectively, where f_{AGN} is the fraction of the observed BBH in the AGN channel. The redshift distribution $f(z)$ we adopt is a model invoking a log-normal delay timescale distribution with respect to star formation history, as applied to the study of SGRBs (Virgili et al. 2011; Sun et al. 2015; Wanderman & Piran 2015). The GW horizon distances for BNS and NSBH mergers in different eras are obtained from Hild et al. (2011), Abbott et al. (2018), Maggiore et al. (2020), and Zhu et al. (2020). By considering the beaming correction factor $f_b \approx (\theta_0 + 1/\Gamma_h)^2/2$ and assuming that all BNS and 20% NSBH mergers (McKernan

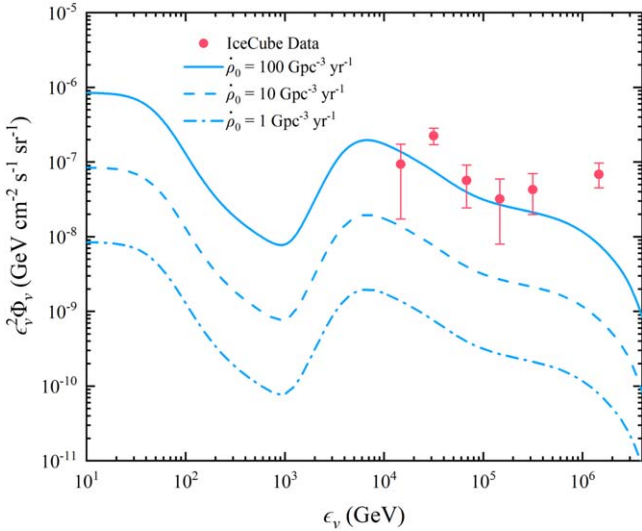


Figure 4. Expected all-flavor diffuse neutrino fluence contributed from choked LGRBs in AGN disks as a function of neutrino energy ϵ_ν . Three local event rates are considered: 100 (solid line), 10 (dashed line), and 1 $\text{Gpc}^{-3} \text{yr}^{-1}$ (dashed-dotted line). The pink circles are the observed diffuse neutrino fluence measured by IceCube (Aartsen et al. 2015a).

et al. 2020) in AGN disks can power classical SGRBs, we show the results of joint GW+neutrino detection rates in Table 1. Such joint detections appear difficult with the current GW and neutrino detectors, but could be possible in the future with next generation GW and neutrino detectors.

5. Neutrino Diffuse Emission

The diffuse neutrino fluence can be estimated as (e.g., Razzaque et al. 2004)

$$\epsilon_{\nu,\text{obs}}^2 \Phi_{\nu,\text{obs}} = \epsilon_{\nu,\text{obs}}^2 f_b \int_0^{z_{\text{max}}} dz \dot{\rho}_0 f(z) F_\nu(\epsilon_{\nu,\text{obs}}) \frac{dV}{dz}, \quad (7)$$

where $\epsilon_{\nu,\text{obs}} = \epsilon_\nu / (1+z)$, and $dV/dz = 4\pi D_L^2 c / (1+z) |dt/dz|$ is the comoving volume element with $(dt/dz)^{-1} = -H_0(1+z) \sqrt{\Omega_\Lambda + \Omega_m(1+z)^3}$. The standard Λ CDM cosmology with $H_0 = 67.8 \text{ km s}^{-1} \text{ Mpc}^{-1}$, $\Omega_\Lambda = 0.692$, and $\Omega_m = 0.308$ (Planck Collaboration et al. 2016) is applied.

In view that the energy of a typical SGRB is much smaller than that of an LGRB and that their event rate density may not be much greater than that of long GRBs, the contribution of choked SGRBs in AGN disks to the neutrino background should be much lower than that of choked LGRBs. We thus only consider the contribution from the latter. Since the cosmic evolution of AGN and star formation rate is not significant (e.g., Madau & Dickinson 2014), we assume that LGRBs in AGN disks are classical LGRBs that closely track the star formation history. We adopt the $f(z)$ distribution based on Yüksel et al. (2008).

We show in Figure 4 the diffuse neutrino fluence by considering three values of the local event rate density due to choked LGRBs in AGN disks are poorly constrained (since these events do not show up as classical GRBs Perna et al. 2021a; Zhu et al. 2021). In an extreme case, if $\dot{\rho}_0 = 100 \text{ Gpc}^{-3} \text{yr}^{-1}$, i.e., comparable to that of low-luminosity GRBs ($\sim 164_{-65}^{+98} \text{ Gpc}^{-3} \text{yr}^{-1}$, Sun et al. 2015), most of the observed neutrino background fluence could be interpreted by

choked LGRBs in AGN disks. If $\dot{\rho}_0 = 10 \text{ Gpc}^{-3} \text{yr}^{-1}$, which is $\sim 5\%$ that of low-luminosity GRBs, the neutrinos from such events can contribute up to $\sim 10\%$ of the observed diffuse neutrino background fluence. Future observations of shock breakout transients from AGN disks (Perna et al. 2021a; Zhu et al. 2021) will better constrain the cosmological event rate density of these choked GRBs in the AGN channel, leading to a better estimation of their contribution to the neutrino background.

6. Discussion

Choked LGRBs and SGRBs in AGN disks are ideal targets for multimessenger observations. Besides neutrino emission discussed in this paper, they can also produce electromagnetic signals from optical to γ -ray bands (Perna et al. 2021a; Zhu et al. 2021). For choked LGRBs, associated SNe could be directly discovered by time-domain survey searches (Assef et al. 2018). Within several years of operation by IceCube and Gen2, neutrino bursts from single events would be possible to be directly detected. Choked SGRBs in AGN disks are emitters of electromagnetic, neutrino, and GW signals. Future joint observations of electromagnetic, neutrino, and GW signals can reveal the existence of this hitherto speculated transient population in AGN disks, shedding light on the interplay between AGN accretion history and the star formation and compact binary merger history in the universe.

Besides classical GRBs from core collapse of massive stars, neutron star mergers, and binary BH mergers (e.g., Bartos et al. 2017; Kaaz et al. 2021; Kimura et al. 2021), accretion of a single BH (Wang et al. 2021), accretion-induced collapse of white dwarfs (J.-P. Zhu et al. 2021, in preparation), and accretion-induced collapse of NSs (Perna et al. 2021b) embedded within AGN disks were also studied recently. Such jets driven by embedded AGN objects could potentially be choked as well and hence produce high-energy neutrinos.

The stalling radius for the jets choked in the AGN disk materials is $\sim 10^{12} - 10^{13} \text{ cm}$. On the other hand, in the traditional GRB model, this radius is also where γ -ray emission is generated (e.g., via internal shocks). However, before the jet breaks out from the star, the jet Lorentz factor is smaller so that internal shock radius would be further in closer to the central engine. Furthermore, as shown by Perna et al. (2021a), in a large parameter space, an external shock into the disk material develops before internal shocks. Even if internal shocks form, γ -ray photons generated in these shocks have a small mean free path due to huge Thompson optical depth of the disk ($\tau_T \approx \rho_0 \sigma_T H / m_p \approx 4 \times 10^3 \rho_{0,-10} H_{14}$). A small fractional of γ -ray photons may be consumed via $p\gamma$ production to produce neutrinos, but most γ -ray photons would be trapped and degraded in energy before escaping the disk. Nonetheless, the cocoon shock breakout from the AGN disk can potentially produce low-luminosity γ -ray emission (Zhu et al. 2021) which has similar observed properties as low-luminosity GRBs. This would happen only if the disk environment at the location where the GRB occurs is less dense while the choked GRB jet is powerful enough. However, γ -ray photons from low-luminosity GRBs are relatively soft ($\lesssim 100 \text{ keV}$; e.g., Campana et al. 2006; Soderberg et al. 2006; Nakar 2015), which are below the energy coverage range of Fermi-LAT (Ackermann et al. 2015). Thus, choked GRB jets in AGN disks do not significantly contribute to the isotropic γ -ray background.

We thank an anonymous referee for thoughtful suggestions. We thank Zhuo Li, Di Xiao, Ming-Yang Zhuang, Yuan-Qi Liu, and Di Zhang for valuable comments. The work of J.P.Z. is partially supported by the National Science Foundation of China under grant No. 11721303 and the National Basic Research Program of China under grant No. 2014CB845800. K.W. is supported by the National Natural Science Foundation under grants 12003007 and the Fundamental Research Funds for the Central Universities (No. 2020kfyXJJS039). Y.P.Y. is supported by National Natural Science Foundation of China grant No. 12003028 and Yunnan University grant No. C176220100087. Y.W.Y. is supported by the National Natural Science Foundation of China under grant No. 11822302, 11833003. H.G. is supported by the National Natural Science Foundation of China under grant No. 11722324, 11690024, 11633001, the Strategic Priority Research Program of the Chinese Academy of Sciences, grant No. XDB23040100 and the Fundamental Research Funds for the Central Universities.

ORCID iDs

Jin-Ping Zhu  <https://orcid.org/0000-0002-9195-4904>
 Kai Wang  <https://orcid.org/0000-0003-4976-4098>
 Bing Zhang  <https://orcid.org/0000-0002-9725-2524>
 Yuan-Pei Yang  <https://orcid.org/0000-0001-6374-8313>
 Yun-Wei Yu  <https://orcid.org/0000-0002-1067-1911>
 He Gao  <https://orcid.org/0000-0002-3100-6558>

References

- Aartsen, M. G., Abraham, K., Ackermann, M., et al. 2015a, *ApJ*, 809, 98
 Aartsen, M. G., Ackermann, M., Adams, J., et al. 2015b, *ApJL*, 805, L5
 Aartsen, M. G., Ackermann, M., Adams, J., et al. 2017, *ApJ*, 843, 112
 Abbott, B. P., Abbott, R., Abbott, T. D., et al. 2017a, *PhRvL*, 119, 161101
 Abbott, B. P., Abbott, R., Abbott, T. D., et al. 2017b, *ApJL*, 848, L13
 Abbott, B. P., Abbott, R., Abbott, T. D., et al. 2017c, *ApJL*, 848, L12
 Abbott, B. P., Abbott, R., Abbott, T. D., et al. 2018, *LRR*, 21, 3
 Abbott, B. P., Abbott, R., Adhikari, R., et al. 2009, *RPPH*, 72, 076901
 Achterberg, A., Gallant, Y. A., Kirk, J. G., & Guthmann, A. W. 2001, *MNRAS*, 328, 393
 Ackermann, M., Ajello, M., Albert, A., et al. 2015, *ApJ*, 799, 86
 Artymowicz, P., Lin, D. N. C., & Wampler, E. J. 1993, *ApJ*, 409, 592
 Assef, R. J., Prieto, J. L., Stern, D., et al. 2018, *ApJ*, 866, 26
 Bartos, I., Kocsis, B., Haiman, Z., & Márka, S. 2017, *ApJ*, 835, 165
 Bellovay, J. M., Mac Low, M.-M., McKernan, B., & Ford, K. E. S. 2016, *ApJL*, 819, L17
 Blandford, R. D., & McKee, C. F. 1976, *PhFl*, 19, 1130
 Bromberg, O., Nakar, E., & Piran, T. 2011a, *ApJL*, 739, L55
 Bromberg, O., Nakar, E., Piran, T., & Sari, R. 2011b, *ApJ*, 740, 100
 Campana, S., Mangano, V., Blustin, A. J., et al. 2006, *Natur*, 442, 1008
 Cantiello, M., Jermyn, A. S., & Lin, D. N. C. 2021, *ApJ*, 910, 94
 Cheng, K. S., & Wang, J.-M. 1999, *ApJ*, 521, 502
 Chodorowski, M. J., Zdziarski, A. A., & Sikora, M. 1992, *ApJ*, 400, 181
 Collin, S., & Zahn, J.-P. 1999, *A&A*, 344, 433
 Denton, P. B., & Tamborra, I. 2018, *ApJ*, 855, 37
 Dittmann, A. J., Cantiello, M., & Jermyn, A. S. 2021, arXiv:2102.12484
 Eichler, D., Livio, M., Piran, T., & Schramm, D. N. 1989, *Natur*, 340, 126
 Fabj, G., Nasim, S. S., Caban, F., et al. 2020, *MNRAS*, 499, 2608
 Fasano, M., Celli, S., Guetta, D., et al. 2021, arXiv:2101.03502
 Fong, W., Berger, E., Margutti, R., & Zauderer, B. A. 2015, *ApJ*, 815, 102
 Galama, T. J., Vreeswijk, P. M., van Paradijs, J., et al. 1998, *Natur*, 395, 670
 Goodman, J., & Tan, J. C. 2004, *ApJ*, 608, 108
 Graham, M. J., Ford, K. E. S., McKernan, B., et al. 2020, *PhRvL*, 124, 251102
 Gupta, N., & Zhang, B. 2007, *Aph*, 27, 386
 Harrison, P. F., Perkins, D. H., & Scott, W. G. 2002, *PhLB*, 530, 167
 Hild, S., Abernathy, M., Acernese, F., et al. 2011, *CQGra*, 28, 094013
 Hjorth, J., Sollerman, J., Møller, P., et al. 2003, *Natur*, 423, 847
 Horváth, I. 2002, *A&A*, 392, 791
 Icecube Collaboration, Abbasi, R., Abdou, Y., et al. 2012, *Natur*, 484, 351
 Jermyn, A. S., Dittmann, A. J., Cantiello, M., & Perna, R. 2021, arXiv:2102.13114
 Kaaz, N., Schröder, S. L., Andrews, J. J., Antoni, A., & Ramirez-Ruiz, E. 2021, arXiv:2103.12088
 Kelner, S. R., Aharonian, F. A., & Bugayov, V. V. 2006, *PhRvD*, 74, 034018
 Keshet, U., & Waxman, E. 2005, *PhRvL*, 94, 111102
 Kimura, S. S., Murase, K., Bartos, I., et al. 2018, *PhRvD*, 98, 043020
 Kimura, S. S., Murase, K., & Bartos, I. 2021, arXiv:2103.02461
 Kouveliotou, C., Meegan, C. A., Fishman, G. J., et al. 1993, *ApJL*, 413, L101
 Kumar, P., & Zhang, B. 2015, *PhR*, 561, 1
 Liang, E., Zhang, B., Virgili, F., & Dai, Z. G. 2007, *ApJ*, 662, 1111
 MacFadyen, A. I., & Woosley, S. E. 1999, *ApJ*, 524, 262
 Madau, P., & Dickinson, M. 2014, *ARA&A*, 52, 415
 Maggiore, M., Van Den Broeck, C., Bartolo, N., et al. 2020, *JCAP*, 2020, 050
 Matzner, C. D. 2003, *MNRAS*, 345, 575
 McKernan, B., Ford, K. E. S., & O’Shaughnessy, R. 2020, *MNRAS*, 498, 4088
 Murase, K. 2007, *PhRvD*, 76, 123001
 Murase, K. 2008, *PhRvD*, 78, 101302
 Murase, K., & Ioka, K. 2013, *PhRvL*, 111, 121102
 Murase, K., & Nagataki, S. 2006, *PhRvD*, 73, 063002
 Nakar, E. 2015, *ApJ*, 807, 172
 Narayan, R., Paczynski, B., & Piran, T. 1992, *ApJL*, 395, L83
 Olive, K. A. & Particle Data Group 2014, *ChPhC*, 38, 090001
 Paczynski, B. 1986, *ApJL*, 308, L43
 Paczynski, B. 1991, *AcA*, 41, 257
 Particle Data Group, Eidelman, S., Hayes, K. G., et al. 2004, *PhLB*, 592, 1
 Patrignani, C., Agashe, K., Particle Data Group, et al. 2016, *ChPhC*, 40, 100001
 Perna, R., Lazzati, D., & Cantiello, M. 2021a, *ApJL*, 906, L7
 Perna, R., Tagawa, H., Haiman, Z., & Bartos, I. 2021b, arXiv:2103.10963
 Planck Collaboration, Ade, P. A. R., Aghanim, N., et al. 2016, *A&A*, 594, A13
 Razzouq, S., Mészáros, P., & Waxman, E. 2004, *PhRvL*, 93, 181101
 Sari, R., & Piran, T. 1995, *ApJL*, 455, L143
 Senno, N., Murase, K., & Mészáros, P. 2016, *PhRvD*, 93, 083003
 Soderberg, A. M., Kulkarni, S. R., Nakar, E., et al. 2006, *Natur*, 442, 1014
 Stanek, K. Z., Matheson, T., Garnavich, P. M., et al. 2003, *ApJL*, 591, L17
 Stecker, F. W. 1968, *PhRvL*, 21, 1016
 Sun, H., Zhang, B., & Li, Z. 2015, *ApJ*, 812, 33
 Tagawa, H., Haiman, Z., & Kocsis, B. 2020, *ApJ*, 898, 25
 Thompson, T. A., Quataert, E., & Murray, N. 2005, *ApJ*, 630, 167
 Virgili, F. J., Zhang, B., O’Brien, P., & Troja, E. 2011, *ApJ*, 727, 109
 Wanderman, D., & Piran, T. 2015, *MNRAS*, 448, 3026
 Wang, J.-M., Ge, J.-Q., Hu, C., et al. 2011, *ApJ*, 739, 3
 Wang, J.-M., Liu, J.-R., Ho, L. C., & Du, P. 2021, arXiv:2103.07708
 Wang, X.-Y., & Dai, Z.-G. 2009, *ApJL*, 691, L67
 Waxman, E., & Bahcall, J. 1997, *PhRvL*, 78, 2292
 Woosley, S. E. 1993, *ApJ*, 405, 273
 Xiao, D., & Dai, Z. G. 2014, *ApJ*, 790, 59
 Xiao, D., Mészáros, P., Murase, K., & Dai, Z.-G. 2016, *ApJ*, 832, 20
 Yu, Y.-W. 2020, *ApJ*, 897, 19
 Yüksel, H., Kistler, M. D., Beacom, J. F., & Hopkins, A. M. 2008, *ApJL*, 683, L5
 Zhang, B. 2018, *The Physics of Gamma-Ray Bursts* (Cambridge: Cambridge Univ. Press)
 Zhang, B., & Kumar, P. 2013, *PhRvL*, 110, 121101
 Zhang, B., & Mészáros, P. 2004, *IJMPA*, 19, 2385
 Zhang, W., Woosley, S. E., & MacFadyen, A. I. 2003, *ApJ*, 586, 356
 Zhu, J.-P., Wu, S., Yang, Y.-P., et al. 2020, arXiv:2011.02717
 Zhu, J.-P., Zhang, B., Yu, Y.-W., & Gao, H. 2021, *ApJL*, 906, L11